Optical spectroscopy noninvasively monitors response of organelles to cellular stress

Georg Schuele
Stanford School of Medicine
Department of Ophthalmology
Stanford, California 94305
and
Stanford University
Hansen Experimental Physics Laboratory
Stanford, California 94305

Edward Vitkin
Harvard Medical School
Beth Israel Deaconess Medical Center
Department of Obstetrics, Gynecology and Reproductive Biology
Biomedical Imaging and Spectroscopy Laboratory
Boston, Massachusetts 02215

Philip Huie
Stanford School of Medicine
Department of Ophthalmology
Stanford, California 94305
and
Stanford University
Hansen Experimental Physics Laboratory
Stanford, California 94305

Caitlin O'Connell-Rodwell
Stanford School of Medicine
Department of Pediatrics, Microbiology & Immunology and Radiology
Stanford, California 94305

Daniel Palanker
Stanford School of Medicine
Department of Ophthalmology
Stanford, California 94305
and
Stanford University
Hansen Experimental Physics Laboratory
Stanford, California 94305

Lev T. Perelman
Harvard Medical School
Beth Israel Deaconess Medical Center
Department of Obstetrics, Gynecology and Reproductive Biology
Biomedical Imaging and Spectroscopy Laboratory
Boston, Massachusetts 02215

Abstract. Fast and noninvasive detection of cellular stress is extremely useful for fundamental research and practical applications in medicine and biology. We discovered that light scattering spectroscopy enables us to monitor the transformations in cellular organelles under thermal stress. At the temperatures triggering expression of heat shock proteins, the refractive index of mitochondria increase within 1 min after the onset of heating, indicating enhanced metabolic activity. At higher temperatures and longer exposures, the organelles increase in size. This technique provides an insight into metabolic processes within organelles larger than 50 nm without exogenous staining and opens doors for noninvasive real-time assessment of cellular stress.
[DOI: 10.1117/1.2075207]

Keywords: thermal stress; light scattering spectroscopy; heat shock protein; retinal pigment epithelium; cellular stress.

Paper SS04199RR received Oct. 22, 2004; revised manuscript received Apr. 26, 2005; accepted for publication Apr. 27, 2005; published online Oct. 13, 2005.

1 Introduction

Transformations of the organelles under conditions of cellular stress are known very little because of their small sizes and low optical contrast. Multiphoton imaging techniques[1] can resolve subcellular structures but require staining to improve the contrast, which often affects cellular metabolism.[2] Electron microscopy provides high resolution but is incompatible with imaging of live cells. Recently, light scattering spectroscopy[3] (LSS) was introduced for noninvasive sizing of organelles in large populations of cells.[4]

The metabolic responses of cells to various stress factors are of great interest to biology and medicine and have been extensively studied. One of the best known responses of cells to stress is the expression of heat shock proteins[5] (HSPs). The

Address all correspondence to Georg Schuele, Lumenis, Inc., 2400 Condensa Street, Santa Clara, CA 95051. Tel: 408–764–3000. Fax: 408–764–3000. E-Mail: schuele@stanford.edu

1083-3668/2005/10(5)/051404/8/$22.00 © 2005 SPIE

HSP expression after thermal stress is the metabolic reaction induced by misaggregation and denaturation of proteins, changes in membrane permeability, and disruption of cytoskeletal components.[6] Initial expression of the heat shock factors[7] (HSFs) regulates the HSP expression, which peaks several hours after the thermal shock.[8]

Several noninvasive techniques have been developed for monitoring cellular metabolism. They rely either on autofluorescence properties,[9] on nonlinear optical polarization,[10,11] or on the scattering properties[12–15] of cells or organelles. Cellular organelles and cell boundaries scatter light with angular and spectral characteristics dependent on the sizes and relative refractive indices of the scattering particles. In general, there are two different approaches to characterize cells by their light scattering. First, the angular distribution of scattering intensity is measured with a goniometer at a fixed wavelength.[16–19] The challenge in this approach is that the signal intensity varies over 5 orders of magnitude, which necessitates the use of a lock-in amplifier. Angular scanning and lock-in techniques are time consuming—typical acquisition times are on the order of several minutes. The second approach, called LSS, measures the back-reflected scattering spectra under well-characterised angles, typically 180±5 deg. The dynamic range of the spectral modulation is typically within one order of magnitude. The amount of reflected light, the integration time of the spectrometer, and its readout limit the acquisition time to typically several hundred milliseconds. Both the goniometer-based approach[17,19] and LSS (Refs. 3 and 4) can extract information about sizes and density of the cellular organelles from the light-scattering data. This information can be used for noninvasive monitoring of the metabolic transformations in cells under any type of cellular stress. As we describe in this paper, the fast data acquisition of LSS enables us to monitor the cellular and subcellular metabolic effects in real time.

Using LSS we studied the reaction of the retinal pigment epithelial (RPE) and NIH-3T3 cells to thermal stress. Motivation for this study comes from the fact that melanosomes within the RPE cells strongly absorb light,[20] and thus the RPE is the hottest layer of cells during laser treatments of the retina.[21] In retinal laser therapies involving prolonged heating, such as transpupillary thermal therapy,[22] the temperature rise in the retina strongly varies from patient to patient due to variation in pigmentation and blood perfusion. Strong differences in temperature result in large variability and poor predictability of the clinical outcomes. A noninvasive on-line dosimetry method is highly desirable to improve this treatment modality.

2 Material and Methods

2.1 *Setup*

A sketch of the setup is shown in Fig. 1. Light from a broadband halogen lamp was coupled into a 3-mm fiber bundle. The fiber tip was imaged 1:1 through a 50% beamsplitter (BS) onto a sample illuminating approximately 10,000 RPE cells within a 3-mm spot. The back-scattered (180±5 deg) light from the sample passing through the 50% BS was directed via an upright microscope (Leica, MZ16) into an optical multichannel analyzer (Ocean Optics, USB2000). A spectrum ranging from 350 to 900 nm and containing 2048 points was typically acquired during 2 s. The sample chamber was placed on

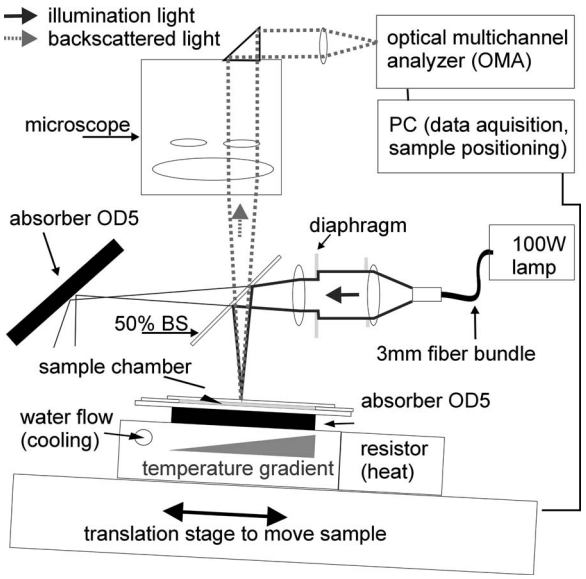

Fig. 1 LSS setup for the detection of temperature-induced cellular stress.

a black light absorbing glass (optical density 5) with glycerine as an index-matching material. To avoid specular reflections from the sample chamber, the whole mount was tilted off the optical axis by several degrees.

The sample mount was heated on one side and cooled on the other side to produce a temperature gradient of about 10°C over a 10-cm distance across the sample. Temperature-time courses for different locations in the sample chamber were measured with a microthermocouple. To measure cellular responses at different temperature courses within the sample the whole mount was moved under the stationary optical setup using a stepper motor. The scattering spectra were acquired every 10 s. The setup was controlled by LabView on a PC.

2.2 *Sample Preparations*

To verify precision in assessment of the sizes and concentrations of the light-scattering particles based on their scattering spectrum, a mixture of polystyrene (PS) beads (Polysciences) of 5 different sizes (291, 585, 737, 1053, and 2105 nm in diameter) was diluted in water at concentration ratio of 5:5:1:1:1, respectively. The light-scattering spectrum was measured and the data were analyzed by the inverse light-scattering fitting algorithm (see Sec. 2.3).

For spectroscopic measurements the human RPE cell line ATCC and the NIH-3T3 cells were confluently grown on glass slides. The NIH-3T3 cells were transfected with a luciferus gene linked to HSP (Ref. 8). The HSP expression from these cells can be detected by imaging (IVIS, Xenogen Corp., Alameda, California, USA) the bioluminescence due to the luciferase activity. During the measurements, the cells were covered with phosphate-buffered solution to avoid light absorption within the colored cell medium, and the sample was covered with a cover slip. To study the reaction of organelles to thermal stress the sample slides were placed on a mount with a temperature gradient ranging from 40 to 50°C. The mount was heated for 15 min and then cooled to room temperature. The scattering spectra were measured at five loca-

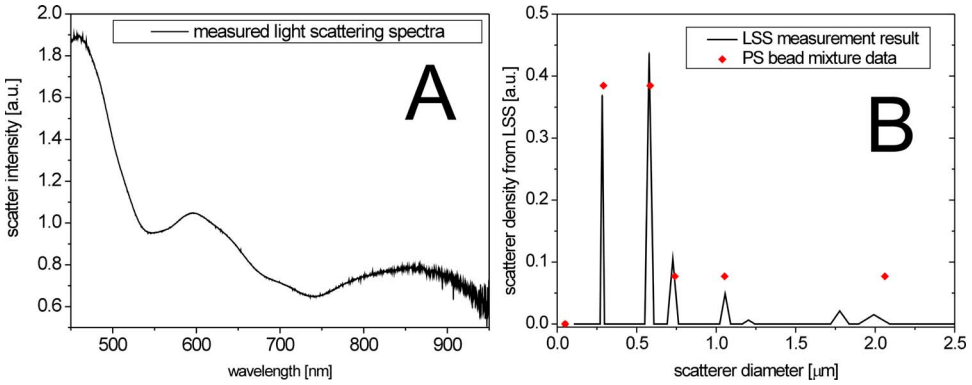

Fig. 2 (a) Light-scattering spectra of a mixture of PS beads with five different sizes ranging from 300 nm to 2 μm, and (b) bead size histogram extracted from the measured scattering spectra. Scatterer density in the histogram represents a product of the $(n-1)^2$ and the number of scatterers (n is the relative refractive index of the particle). Since the refractive index is the same for all beads, the plot represents the relative number of particles. The diamonds in (b) depict the real composition of the PS bead mixture. The bead sizes can be determined far below the optical resolution of a conventional microscope—down to 50 nm.

tions on the slides corresponding to five different temperatures within this range. After the experiments, all cells were alive as indicated by the live/dead calceinAM and ethidium homodimer fluorescent assay.[23]

For histological study with transmission electron microscopy (TEM) the RPE cells were grown on a Mylar film. After fixation with 2.5% glutaraldehyde/1% paraformaldehyde, embedding in LX-112, and staining in uranyl acetate/lead citrate, the 200-nm-thick sections were examined under TEM. The distribution of sizes of different organelles in the TEM photographs were analyzed using the ImageJ software.[24]

2.3 *Inverse Light-Scattering Fitting Algorithm*

In a single scattering approximation, the scatterer size density distributions $N(D)$ were extracted from the measured scattering spectra using the following Mie theory-based approach. If incident light is scattered by the particles of various diameters D, the scattered light intensity can be expressed as an integral over all diameters:

$$I = I_0 C \int N(D)\,\mathrm{d}D \int_0^{\theta_0}\int_0^{2\pi} \sin\theta_i\,\mathrm{d}\theta_i\,\mathrm{d}\varphi_i \int_0^{\theta_0}\int_0^{2\pi} \sin\theta_s\,\mathrm{d}\theta_s\,\mathrm{d}\varphi_s \times\left[\left|S_1(\theta,n,D,\lambda)\right|^2 + \left|S_2(\theta,n,D,\lambda)\right|^2\right], \quad (1)$$

where I_0 is the intensity of the incident wave; C is the apparatus constant of the system; θ_0 is the delivery/collection angle of the system; θ is the scattering angle, which depends on the angles of incoming light θ_i, φ_i, and the angles of the scattered light θ_s and φ_s; and $S_1(\theta,n,D,\lambda)$ and $S_2(\theta,n,D,\lambda)$ are diagonal elements of the scattering matrix at given wavelength λ and relative refractive index $n=n_s/n_0$, where n_s is the refractive index of the scatterer and n_0 is the refractive index of the surrounding medium. The elements of the scattering matrix are calculated using Mie theory.[25]

Equation (1) relates the intensity spectrum of scattered light $I(\theta,n,D,\lambda)$ to the scattering amplitudes $S_1(\theta,n,D,\lambda)$ and $S_2(\theta,n,D,\lambda)$. In backscattering direction, the spectrum $I(\theta,n,D,\lambda)$ of a submicrometer particle with the relative refractive index close to unity has unique modulations, which depend on the scatterer diameter D and scales proportionally to $(n-1)^2$. The light scattering spectra of particles smaller than 50 nm are featureless, and Mie theory approximates to a classical Rayleigh scattering.[26] The scatterer size density distribution $N(D)$ for sizes larger than 50 nm can thus be extracted by fitting[27] the predictions of the model to the measured scattering spectrum. We developed such automated inversion procedure, which extracts the size density histogram of the scatterers that best fit the measured light scattering spectrum.[4] The relative refractive index of subcellular organelles used for these calculations[28] was $n=1.04$, and for the PS beads, $n=1.20$. The code is written in Fortran and runs reasonably fast ($\sim$10 s/spectrum) on a conventional PC (Pentium, 2 GHz, Windows).

3 Results

3.1 *Measurements on Polystyrene Bead Mixtures*

To verify precision in assessment of the sizes and relative scatterer concentrations the sample cuvette was filled with the PS beads mixture and the light scattering spectrum was measured [Fig. 2(a)]. The histogram of sizes in the PS bead mixture was extracted from this spectrum [Fig. 2(b)] by the inverse light-scattering fitting algorithm. Scatterer density in the histogram represents a product of the $(n-1)^2$ (where n is relative refractive index of the particle) and the number of scatterers.[4]

3.2 *Sizing of Cellular Organelles*

To validate the LSS assessment of the sizes of cellular organelles, the light-scattering spectrum of RPE cells was measured at 37 °C [Fig. 3(a)], and the scatterer density histogram was extracted from this spectrum using the inverse light scattering algorithm (Sec. 2.3). To make the results of LSS comparable to the size distribution observed in histological sections, the scatterer density histogram was converted into a histogram representing a statistical distribution of cross sections of organelles in the arbitrarily oriented sections of 200 nm in thickness. The area under this transformed histogram was normalized to 1 [full circular symbols in Fig. 3(b)].

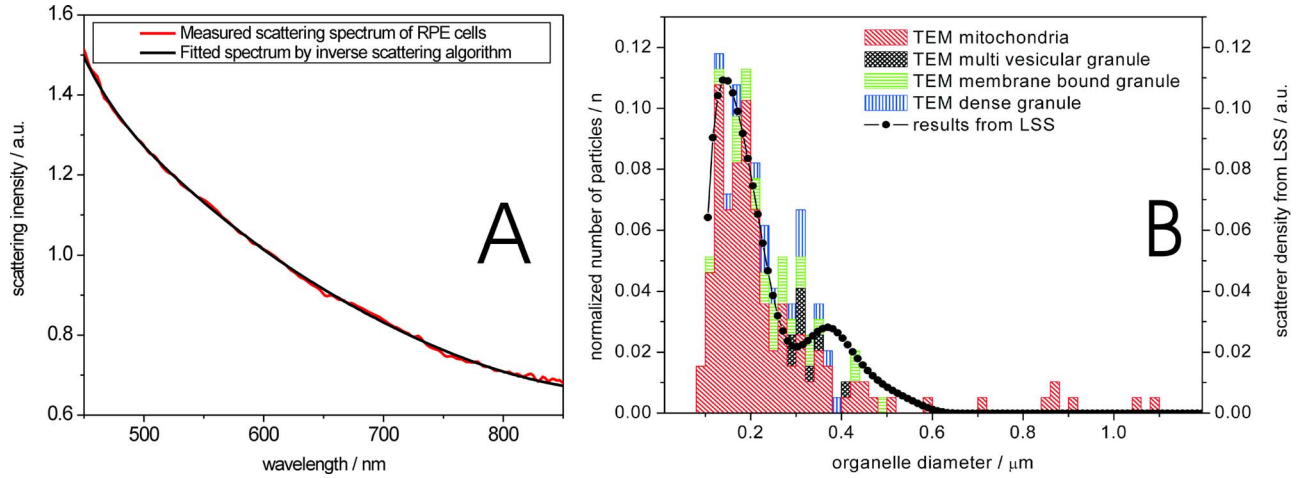

Fig. 3 (a) Light-scattering spectrum of RPE cells and the spectrum fitted with the inverse light-scattering algorithm and (b) the maximum and minimum dimension of the different types of organelles was determined on 50 TEM histological sections (200 nm thick) of RPE cells. The area under the organelle size histogram was normalized to 1 (hatched areas). The line with the circular symbols represents the data extracted from the light scattering spectrum. The histogram was transformed from a 3-D particle size distribution into a histogram of arbitrarily oriented slices of 200 nm in thickness.

The maximum and minimum dimensions of the different organelles were determined in 50 TEM sections (200 nm thickness) of RPE cells using ImageJ software. The resulting organelle size histogram was then normalized to an area of one [hatched area in Fig. 3(b)]. It is important to keep in mind that the conversion of the histograms from 3-D particles into a histogram of 2-D slices resulted in a slight shift of their maxima to smaller sizes. The actual sizes of the 3-D organelles peak at 170 and 385 nm rather than 150 and 365 nm, respectively.

3.3 *Optical Detection of Cellular Stress*

In experiments with cells, the spectral changes appeared within 1 min after the onset of heating. The heat-induced changes in the scattering spectra [Fig. 4(a)] were more pronounced in the long-wavelength region. The scatterer density histograms [Fig. 4(b)] extracted from the measured spectra [shown in Fig. 4(a)] demonstrate that the scattering density of the 170-nm mitochondria increased very significantly (up to 50%) and the distribution slightly shifts (up to 15 nm) toward the larger sizes.

Figure 5(a) shows the time course of the maximum scattering density for different temperatures. The dashed line indicates the heating time course; in this case, for 50°C. The scattering density starts increasing at 42.5°C and exhibits strongest response at 45°C, reaching its maximum at about 16 min. After the heat is turned off, the scattering intensity does not decrease to its original value [Fig. 5(a)]. At a higher temperature, 47°C, the organelles react faster, reaching the peak at about 6 min, but after that the scattering density is decreasing. At 50°C, the scattering density increase is even smaller than at 45 and 47.5°C. Starting at temperatures of 47.5°C, the density peak shifts up to 15 nm toward larger sizes [Fig. 5(b)] and the width of the distribution increases (not shown). Both of these effects become most pronounced at the highest temperature of 50°C. All cells were still viable

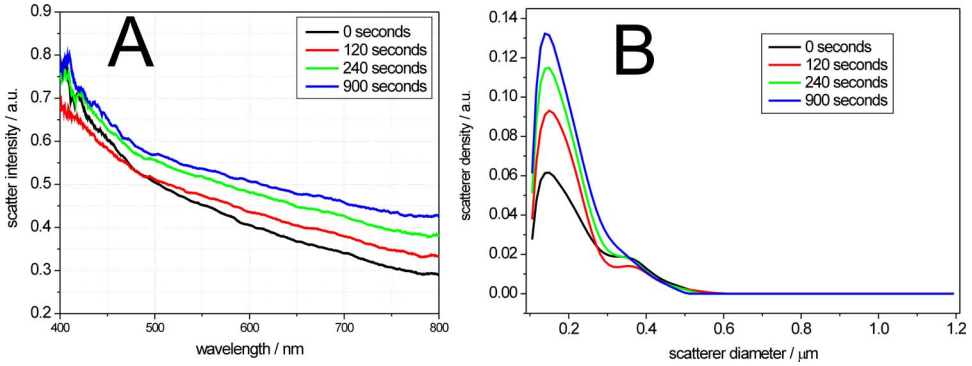

Fig. 4 (a) Light-scattering spectra of the RPE cells at different moments of time under thermal stress of 47.5°C, where the temperature-induced spectral changes are more pronounced in the long-wavelength region, and (b) corresponding histograms of the scatterer density extracted from the spectra. Amplitude of the 160-nm peak in the histogram strongly increases during heating, while its position slightly shifts toward larger sizes. Increase in the amplitude represents the rise of the refractive index of the organelles probably due to the enhanced metabolic activity.

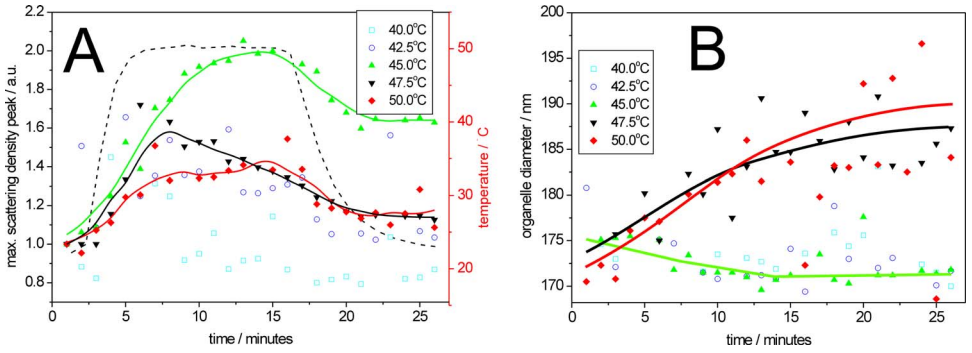

Fig. 5 (a) Time course of the maximum scatterer density (i.e., relative refractive index) of the RPE organelles at different maximal temperatures. The temperature course of the 50.0°C point on the sample is plotted as a dashed line with the temperature scale on the right. A slight increase of the scattering density can be seen for 42.5°C, and it reaches its maximum at 45.0°C. The increase starts earlier at higher temperatures. Interestingly, at 50°C the increase in scattering density is less pronounced than at 47.5 and 45.0°C, indicating that metabolic response is suppressed. (b) Time course of the mitochondrial width at different maximal temperatures. The width increases with time by about 15 nm at temperatures of 47.5 to 50.0°C.

immediately after the heating, as proved by the live/dead fluorescent assay.[23]

The extracted scatterer density histograms of the NIH-3T3 cells were similar to the histograms obtained with the RPE cells [shown in Fig. 3(b)]. Figure 6(a) shows the temporal course of the scattering density at the 170-nm position of the peak. The time course of the actual temperature on a sample in a position corresponding to the maximal temperature of 45°C is shown as a dashed line. The NIH-3T3 cells respond differently than RPE cells: they start reacting at lower temperatures, 41°C, and have much slower rise of the scattering density reaching its maximum only by the end of the heating cycle, at 16 min for all the temperatures above 41°C. At higher temperatures (43 and 45°C), they react a little faster, but as opposed to the RPE cells, for all temperatures the scattering density decreases by the end of the cooling phase. No size shift of the maximum scattering density or broadening of the size distribution was found with NIH-3T3 cells in the examined temperature range up to 45°C.

To compare our findings regarding response of organelles to thermal stress we studied expression of the HSP in the NIH-3T3 cells under the same experimental conditions. Figure 6(b) shows the light emission by the luciferase linked to HSP 6 h after heating. The peak of the HSP expression was observed at 43°C.

4 Discussion

4.1 *Assessment of Diameters and Concentrations of PS Beads in Mixture*

PS beads are a commonly used model system for light-scattering experiments. Their optical properties and spherical shape is well defined and they can be purchased in sizes ranging from 40 nm to hundreds of micrometers. Several authors describe the successful extraction of PS bead diameters using only one size at a time. In previous studies, either arbitrary chosen normal[3,4,13] or a log-normal Gaussian[19] size distribution were assumed to reduce the number of free parameters during the fit. In our experiments, we used a mixture of PS beads with sizes ranging from 300 nm to up to 2.1 μm, imitating the fact that cells contain organelles with a broad range of sizes. Therefore, we did not assume any specific type of size distribution in our inverse light-scattering code.

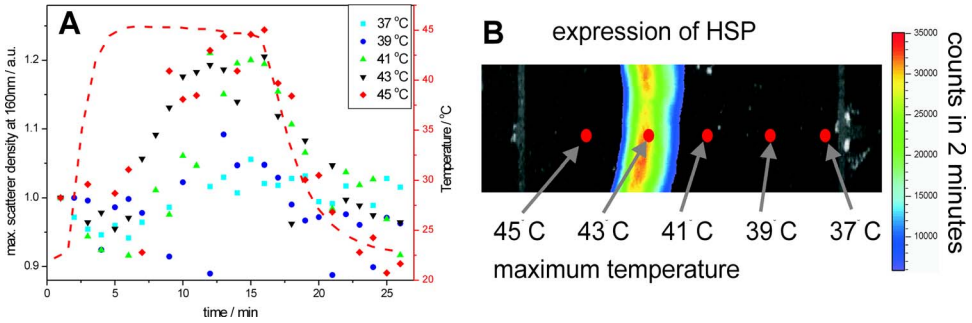

Fig. 6 (a) Time course of the scatterer density of the 170-nm organelles in the NIH-3T3 cells for different maximal temperatures. The time course of the 45°C point is plotted with a dashed line (temperature scale on the right). Significant increase of the scattering density starts at 41°C. The onset of this effect is earlier at higher temperatures. No significant changes of the scatterer sizes were observed at these temperatures. (b) Expression of HSP measured by light emission of luciferase 6 h after the exposure. The dots mark the areas with different temperatures where the scattering spectra were acquired. The HSP expression peaks at 43°C.

Figure 2(b) demonstrates a good correspondence between the actual mixture composition (filled diamonds) and the size distribution (solid line) extracted from the scattering spectra shown in Fig. 2(a). It is remarkable that small particles are clearly resolved with this technique far beyond the optical resolution of a conventional light microscope. The extracted sizes of the beads correspond to actual sizes with precision of ±10 nm, except for one broadened peak in the proximity of 2 μm. Scattering from the larger particles, which has the fastest spectral modulation, are optically suppressed in our cuvette: 0.43% of the transmitted light is reflected back from the bottom of the cuvette. To prevent specular reflection from entering the microscope objective the sample holder was slightly tilted. However, the forward scattering of this light in the sample is quite strong, especially for large particles, and it was collected into the spectrometer. The forward-scattering spectrum does not exhibit any significant spectral modulation, and this signal lowers the sensitivity of the technique for larger particles. This effect is reflected in nonprecise determination of the particle sizes around 2 μm, as shown in Fig. 2(b).

The precision of LSS in absolute measurement of sizes and its ability to monitor small relative changes are not the same. The absolute precision of sizing is defined as the deviation of the reconstructed size from the bead size data provided by a manufacturer. However, three types of the errors can affect this: the model-related error, the error of the size determination by the manufacturer, and the error related to the experimental SNR. Precision in detecting the relative size changes [e.g., Fig. 5(b)] should be much higher than the precision of absolute size determination since it is not affected only by the model-related error and depends only on the SNR. In fact, precision in determination of the relative change in organelle sizes is equal to the SNR. For 200-nm particles and a 100:1 SNR the relative accuracy will thus be around 2 nm.

4.2 *Assessment of Cellular Organelle Size Distribution*

There is no "gold standard" technique for sizing of cellular organelles. In general, only TEM provides the necessary resolution, but it comes at a cost of complete disruption of the cellular metabolism due to fixation, embedding, and cutting. Some changes in organelle sizes and shape during fixation and embedding cannot be excluded.

The peak around 170 nm in Fig. 3(b) corresponds primarily to a cross section of mitochondria, with sizes ranging from 90 to 500 nm. The mean width of the mitochondria found in this study is slightly smaller than the 250 nm reported in the literature.[19] Other types of organelles such as multivesicular granules (polysomes, intermediate filaments, microtubules, secondary lysosomes[29]), membrane-bound granules (lysosomes[29]), and dense granules (phagosomes in the end-stage of hydrolic digestion[29]) are also found in the size range from 160 to 450 nm with a peak around 340 nm. The scatterer size distribution [filled dots in Fig. 3(b)] extracted from the scattering spectra also has two distinct peaks at 170 and 380 nm.

The good agreement between the extracted scatterer density histogram and the TEM analysis for cellular organelles, which generally are not spherical, supports the validity of the spherical approximation for this type of scatterers. A more complex modeling that can include different shapes, such as the T-Matix method,[30] could lead to more precise results, but will also add some free parameters.

In the past, we studied contributions of large organelles, such as cell nuclei[3] and smaller, submicrometer organelles such as peroxisomes and lysosomes.[4] In an intact biological cell, both large and small organelles contribute to the overall LSS spectrum. However, those contributions have distinct characteristics that make it relatively simple to analyze large and small organelles separately. The nucleus, being a larger particle, has a stronger oscillatory component in the LSS spectrum, which is preserved even after averaging over a large number of nuclei of different sizes present in the illuminated volume. Smaller organelles have a significantly smoother spectrum with no prominent oscillations present. The LSS scattering spectrum from epithelial cells *in vivo*[31] is dominated by a strong diffuse background coming from multiple scattering in the underlying tissue. This component can be removed to reveal features related to the cell nuclei. However, since it is rather difficult to differentiate the smooth spectrum generated by small organelles from the equally smooth diffuse background spectrum, both components are normally removed in the same procedure. In the individual cells on a glass slide, there is no diffuse background and contribution of the small organelles is much easier to observe. Thus, not only the nuclear sizes but also the sizes of the small organelles can be extracted.

In this study, contributions from the nuclei are very small because of the particular geometry chosen for the measurements. The RPE and NIH-3T3 cells used in the experiments were confluently grown on a glass slide. The TEM photographs revealed that their height is only around 1.3 μm, but the width is around 10 to 15 μm. To prevent specular reflection from entering the microscope objective the sample was slightly tilted. This also drastically reduced the contribution from the "flat" surfaces of the nuclei, which have the same orientation as a glass slide. As a result, modulations with high spectral frequency produced by nuclei have very low intensity and can hardly be seen as a residual from our LSS fit in Fig. 3(a). At the same time, the reconstruction algorithm when applied to this residual reveals two peaks at around 1.5 and 10 μm.

4.3 *Detection of Cellular Stress*

The light scattering properties of cells are known to change during cell proliferation,[17] apoptosis,[14] toxic stress,[32,33] and osmotic shock.[34] Using LSS, the subcellular origin and the specific organelles associated with these effects can now be identified and monitored in real time.

As shown in Fig. 4(a), the spectral response for RPE cells is smooth and more pronounced at the longer wavelengths. The size histograms [Fig. 4(b)] extracted from these data show a strong increase in scattering density of the 170-nm organelles. The scatterer density represents a product of the $(n-1)^2$ (where n is a relative refractive index of the particle) times the number of particles.[4] Since organelles cannot multiply on such a short time scale, this increase in the scatterer density is due to the rise of the refractive indices of the organelles. This reaction can be associated with the histologically known "mitochondrial pyknosis,"[35,36] an increase in op-

tical density of the mitochondria matrix[37] due to the thermal stress. As shown in Fig. 5(a), the onset and the temporal behavior of this reaction can now be followed in real time. For RPE cells, the changes begin around 42.5°C and are strongest at 45°C. The earlier but lower response at 47.5 and 50°C probably indicate at suppressed metabolism at higher temperatures. In the NIH-3T3 cells [Fig. 6(a)], an increase of scattering density has already begun at 41°C, but these cells react much more slowly than RPE cells—the onset was delayed by 5 to 10 min, and similarly for RPE cells, it begins earlier at higher temperatures. The fact that these reactions do not follow the temperature history in the sample indicates that we observe the effects of cellular metabolic activity rather than just the temperature dependence of the refractive indices of the organelles.

As shown in Fig. 6(b), the HSP expression on the heated sample slide peaked at the location heated to 43°C. An increase of the mitochondria scattering density in the same sample was found at 41°C. Thus, in addition to ability of detecting cellular stress noninvasively and in real time, the mitochondrial pyknosis seems to be an even earlier indicator than the expression of HSP.

Figure 5(b) shows that swelling of the RPE mitochondria begins at 47.5°C. This effect corresponds to histological observations of the swelling of the mitochondrial matrix at the beginning of apoptosis,[35] which is expected at these temperatures.[38–40]

5 Conclusions

This paper demonstrated that LSS enables the noninvasive sizing of cellular organelles, and can be successfully used for rapid and noninvasive monitoring of the early subcellular transformations in living cells under thermal stress. With LSS, the subcellular origin and the specific organelles associated with these effects can now be identified and monitored in real time. This technique can be applied to organelles with dimensions down to 50 nm, and opens doors to quantitative real-time assessment of the organelle reactions to various types of cellular stress without exogenous staining or labeling.

An increase of mitochondrial scattering density with temperature (correlating with histological observation of "mitochondrial pyknosis") begins below the temperatures corresponding to maximal expression of HSP, and can probably be used as an early indicator of thermal stress. Swelling of the mitochondria was found at temperatures above the HSP expression threshold, and can be associated with the onset of cellular apoptosis.

Noninvasive monitoring of cellular stress with LSS can be used for a real-time dosimetry in a wide variety of medical applications that have no immediate observable outcome, such as transpupillary thermal therapy, photodynamic therapy, and electroporation. It might also be useful for environmental monitoring of toxins, drug screening, and others biotechnological purposes. Future studies must prove the specificity and sensitivity of this technique in each application.

References

1. S. W. Hell, "Toward fluorescence nanoscopy," *Nat. Biotechnol.* **21**(11), 1347–1355 (2003).
2. W. T. Mason, *Fluorescent and Luminescent Probes for Biological Activity*, Academic Press (1999).
3. L. T. Perelman, V. Backman, M. Wallace, G. Zonios, R. Manoharan, A. Nusrat, S. Shields, M. Seiler, C. Lima, T. Hamano, I. Itzkan, J. Van Dam, J. M. Crawford, and M. S. Feld, "Observation of periodic fine structure in reflectance from biological tissue: a new technique for measuring nuclear size distribution," *Phys. Rev. Lett.* **80**(3), 627–630 (1998).
4. H. Fang, M. Ollero, E. Vitkin, L. M. Kimerer, P. B. Cipolloni, M. M. Zaman, S. D. Freedman, I. J. Bigio, I. Itzkan, E. B. Hanlon, and L. T. Perelman, "Noninvasive sizing of subcellular organelles with light scattering spectroscopy," *IEEE J. Sel. Top. Quantum Electron.* **9**(2), 267–276 (2003).
5. J. G. Kiang, and G. C. Tsokos, "Heat shock protein 70 kDa: molecular biology, biochemistry, and physiology," *Pharmacol. Ther.* **80**(2), 183–201 (1998).
6. L. A. Sonna, J. Fujita, S. L. Gaffin, and C. M. Lilly, "Invited review: effects of heat and cold stress on mammalian gene expression," *J. Appl. Physiol.* **92**(4), 1725–1742 (2002).
7. L. Pirkkala, P. Nykanen, and L. Sistonen, "Roles of the heat shock transcription factors in regulation of the heat shock response and beyond," *FASEB J.* **15**(7), 1118–1131 (2001).
8. C. E. O'Connell-Rodwell, D. Shriver, D. M. Simanovskii, C. McClure, Y. A. Cao, W. Zhang, M. H. Bachmann, J. T. Beckham, E. D. Jansen, D. Palanker, H. A. Schwettman, and C. H. Contag, "A genetic reporter of thermal stress defines physiologic zones over a defined temperature range," *FASEB J.* **18**(2), 264–271 (2004).
9. B. Chance, "Mitochondrial NADH redox state, monitoring discovery and deployment in tissue," *Methods Enzymol.* **385**, 361–370 (2004).
10. P. J. Campagnola, H. A. Clark, W. A. Mohler, A. Lewis, and L. M. Loew, "Second-harmonic imaging microscopy of living cells," *J. Biomed. Opt.* **6**(3), 277–286 (2001).
11. J.- X. Cheng and X. S. Xie, "Coherent anti-stokes Raman scattering microscopy: instrumentation, theory, and applications," *J. Phys. Chem. B* **108**, 827–840 (2004).
12. E. Sobol, A. Sviridov, M. Kitai, J. M. Gilligan, N. H. Tolk, and G. S. Edwards, "Time-resolved, light scattering measurements of cartilage and cornea denaturation due to free electron laser radiation," *J. Biomed. Opt.* **8**(2), 216–222 (2003).
13. V. Backman, M. B. Wallace, L. T. Perelman, J. T. Arendt, R. Gurjar, M. G. Muller, Q. Zhang, G. Zonios, E. Kline, J. A. McGilligan, S. Shapshay, T. Valdez, K. Badizadegan, J. M. Crawford, M. Fitzmaurice, S. Kabani, H. S. Levin, M. Seiler, R. R. Dasari, I. Itzkan, J. Van Dam, M. S. Feld, and T. McGillican, "Detection of preinvasive cancer cells," *Nature (London)* **406**(6791), 35–36 (2000).
14. Z. Shiffer, N. Zurgil, Y. Shafran, and M. Deutsch, "Analysis of laser scattering pattern as an early measure of apoptosis," *Biochem. Biophys. Res. Commun.* **289**(5), 1320–1327 (2001).
15. N. N. Boustany, R. Drezek, and N. V. Thakor, "Calcium-induced alterations in mitochondrial morphology quantified in situ with optical scatter imaging," *Biophys. J.* **83**(3), 1691–1700 (2002).
16. J. R. Mourant, J. P. Freyer, A. H. Hielscher, A. A. Eick, A. Shen, and T. M. Johnson, "Mechanisms of light scattering from biological cells relevant to noninvasive optical-tissue diagnostics," *Appl. Opt.* **37**(16), 3586–3593 (1998).
17. J. R. Mourant, M. Canpolat, C. Brocker, O. Esponda-Ramos, T. M. Johnson, A. Matanock, K. Stetter, and J. P. Freyer, "Light scattering from cells: the contribution of the nucleus and the effects of proliferative status," *J. Biomed. Opt.* **5**(2), 131–137 (2000).
18. J. R. Mourant, T. M. Johnson, V. Doddi, and J. P. Freyer, "Angular dependent light scattering from multicellular spheroids," *J. Biomed. Opt.* **7**(1), 93–99 (2002).
19. J. D. Wilson, C. E. Bigelow, D. J. Calkins, and T. H. Foster, "Light scattering from intact cells reports oxidative-stress-induced mitochondrial swelling," *Biophys. J.* **88**, 2929–2938 (2005).
20. Macular Photocoagulation Study Group, "Laser photocoagulation of subfoveal recurrent neovascular lesions in age-related macular degeneration. Results of a randomized clinical trial," *Arch. Ophthalmol. (Chicago)* **109**(9), 1232–1241 (1991).
21. M. A. Mainster, T. J. White, J. H. Tips, and P. W. Wilson, "Retinal-temperature increases produced by intense light sources," *J. Opt. Soc. Am.* **60**(2), 264–270 (1970).
22. M. A. Mainster and E. Reichel, "Transpupillary thermotherapy for age-related macular degeneration: long-pulse photocoagulation, apoptosis, and heat shock proteins," *Ophthalmic Surg. Lasers* **31**(5), 359–373 (2000).

23. Molecular Probes, "*LIVE/DEAD Viability/Cytotoxicity*," *product information* (2001).
24. W. Rusband, *ImageJ 1.32*. 2004, National Institute of Health.
25. G. Mie, "Beitraege zur Optik trueber Medien, speziell kolloidaler Metalloesungen," *Ann. Phys.* **29**, 377–445 (1908).
26. C. F. Bohren and D. R. Huffman, *Absorption and Scattering of Light by Small Particles*, Wiley, New York (1998).
27. IMSL, "*DLCLSQ: Linear least-square problems with linear constrains*," *in DLCLSQ: Linear Least-Square Problems with Linear Constrains*, Visual Numerics IMSL, San Ramon (2003).
28. L. T. Perelman and V. Backman, "*Light scattering spectroscopy of epithelial tisuues: principles and applications*," in *Handbook on Optical Biomedical Diagnostics*, V. Tuchin, Ed., pp. 675–724, SPIE Press, Bellingham, WA (2002).
29. M. Hogan, J. A. Elvarado, and J. E. Wedell, *Histology of the Human Eye*, Saunders, Philadelphia (1971).
30. M. I. Mishchenko, L. D. Travis, and D. W. Mackowski, "T-matrix computations of light scattering by nonspherical particles: a review," *J. Quant. Spectrosc. Radiat. Transf.* **55**(5), 535–575 (1996).
31. V. Backman, R. Gurjar, K. Badizadegan, I. Itzkan, R. R. Dasari, L. T. Perelman, and M. S. Feld, "Polarized light scattering spectroscopy for quantitative measurement of epithelial cellular structures in situ," *IEEE J. Sel. Top. Quantum Electron.* **5**(4), 1019–1026 (1999).
32. D. N. Georgieva, N. Genov, K. Hristov, K. Dierks, and C. Betzel, "Interactions of the neurotoxin vipoxin in solution studied by dynamic light scattering," *Biophys. J.* **86**(1, Pt.1), 461–466 (2004).
33. B. V. Bronk, Z. Z. Li, and J. Czege, "Polarized light scattering as a rapid and sensitive assay for metal toxicity to bacteria," *J. Appl. Toxicol.* **21**(2), 107–113 (2001).
34. S. P. Srinivas, J. A. Bonanno, E. Lariviere, D. Jans, and W. Van Driessche, "Measurement of rapid changes in cell volume by forward light scattering," *Pfluegers Arch. Gesamte Physiol. Menschen Tiere* **447**(1), 97–108 (2003).
35. S. Desagher and J. C. Martinou, "Mitochondria as the central control point of apoptosis," *Trends Cell Biol.* **10**(9), 369–377 (2000).
36. C. R. Hackenbrock, "Chemical and physical fixation of isolated mitochondria in low-energy and high-energy states," *Proc. Natl. Acad. Sci. U.S.A.* **61**(2), 598–605 (1968).
37. B. A. Scalettar, J. R. Abney, and C. R. Hackenbrock, "Dynamics, structure, and function are coupled in the mitochondrial matrix," *Proc. Natl. Acad. Sci. U.S.A.* **88**(18), 8057–8061 (1991).
38. K. Li, Y. Li, J. M. Shelton, J. A. Richardson, E. Spencer, Z. J. Chen, X. Wang, and R. S. Williams, "Cytochrome c deficiency causes embryonic lethality and attenuates stress-induced apoptosis," *Cell* **101**(4), 389–399 (2000).
39. M. G. Vander Heiden, N. S. Chandel, P. T. Schumacker, and C. B. Thompson, "Bcl-xL prevents cell death following growth factor withdrawal by facilitating mitochondrial ATP/ADP exchange," *Mol. Cell* **3**(2), 159–167 (1999).
40. G. Kroemer, "Mitochondrial control of apoptosis: an introduction," *Biochem. Biophys. Res. Commun.* **304**(3), 433–435 (2003).